

Flow Topology and Secondary Separation Modelling at Crossing Shock Wave/Turbulent Boundary Layer Interaction Conditions

Andrea Salin ^a, Yufeng Yao ^a and Alexander A. Zheltovodov ^b

^aSchool of Aerospace and Aircraft Engineering, Kingston University, London SW15 3DW, UK

^bKhrstianovich Institute of Theoretical and Applied Mechanics Siberian Branch of Russian Academy of Sciences, Novosibirsk 630090, Russia

Abstract

Steady RANS modelling has been carried out for a symmetrical double-sharp-fin configuration with an inclination angle 15° , Mach 3.92 and Reynolds number $Re_\delta = 3.08 \times 10^5$. Grid refinement and turbulence model influences using ω -based Reynolds Stress model (RSM), one-equation Eddy Viscosity Transport and two-equation Shear Stress Transport, have been studied and predicted wall pressure distributions were in good agreement with experiment data. RSM model surface flow topology was found to be in better qualitative agreement with experimental oil-flow visualization than those from other two models. The secondary separation phenomenon observed in the experiment was successfully reproduced by the RSM model, due to its ability to evaluate correct level of turbulence kinetic energy that is critical in determining pseudo-laminar state of an embedded reversed flow underneath the main cross-flow vortex. Three-dimensional flow structures demonstrated that the initially weak secondary separation has been further strengthened in span-wise direction towards the central separated zone.

1. INTRODUCTION

In order to reproduce shock-wave/turbulent-boundary-layer interactions (SWTBLI) in high-speed flows, a simple configuration of double fin (DF) mounted on a flat plate (see Figure 1), has been adopted in several experimental and numerical investigations over the last decades. This configuration simulates a generic high-speed sidewall compression inlet in which a pair of crossing shock waves interacts with each other, and also with an incoming supersonic turbulent boundary layer on the bottom wall. One of primary goals for an efficient air-breathing high-speed inlet design is to effectively control the three-dimensional (3-D) SWTBLI, and thus to provide nearly uniform flow with higher total pressure at the engine combustion chamber. However, possible appearance of the boundary layer separation zones, due to strong shock/boundary-layer interactions, will stimulate the total pressure losses and high wall heat fluxes concentrated in some wall regions which can cause serious structural damages and possibly lead to the engine “un-start” phenomena in the worst situation.

Review papers by Knight et al. [1], Zheltovodov [2], and Zheltovodov and Knight [3] provided summary of current state-of-the-art of research advancements in the field of SWTBLI. Overall, these surveys emphasized that while increasing the crossing-shock-wave/turbulent-boundary-layer interaction (CSWTBLI) strengths, the surface pressure and heat transfer coefficients were systematically over-predicted by numerical simulations, as well as some discrepancies appeared on the surface flow topology. One of the key reasons of these disagreements was the inaccuracy of resolving the near-wall flow properties by most eddy viscosity based algebraic and/or two-equation turbulence models (see, e.g. [4, 5, 6]). In fact, isotropic linear eddy viscosity models such as two-equation models have been found to largely overestimate the turbulence kinetic energy (TKE) level in the vicinity of wall regions by at least one-order of magnitude. As a result, computation using these models was often

unable to capture secondary flow separation lines at moderate interaction strength; a phenomenon observed by experiments and believed to be associated with a pseudo-laminar boundary-layer separation. Furthermore, the wall bounded properties such as skin friction and wall heat transfer coefficients were also systematically overestimated and for the latter, discrepancy between numerical prediction and experimental test can be more than 50%.

The interactions of the 3-D inviscid swept shock wave generated from sharp fin leading-edge with incoming supersonic turbulent boundary-layer can result in a viscous flow separation due to strong adverse pressure gradients (APG) produced during the formation of a λ -foot shock and more complex flow field structure may arise in the vicinity of the crossing swept shock waves [1, 2, 3]. Experiments on a single fin (SF) configuration evidenced the vortical nature of the flow embedded within the λ -foot shock structure and a classification of the so-called secondary separation development stages has been established by Zheltovodov [7] (see, additionally [1, 2, 3]). According to this classification, secondary separation appears underneath the primary vortical flow when interaction reaches moderate/strong shock strength, then it disappears and reappears again in very strong shock-wave/turbulent-boundary-layer interactions. To the authors' knowledge, there are limited successful numerical investigations in the past in predicting the secondary separation phenomenon for both single-fin and double-fin configurations. The earliest study of a single-fin (SF) configuration was carried out by Panaras [8] using a steady Reynolds-averaged Navier-Stokes (RANS) approach with a modified algebraic Baldwin-Lomax (BL) model and the secondary separation phenomenon in a moderate interaction regime was numerically reproduced for the first time. By implementing the minimal weakly non-linear correction of Durbin [9] into the Wilcox $k-\omega$ model, Thivet et al. [10] also numerically reproduced the secondary separation in a very strong interaction single-fin configuration case (Mach 4, wedge angle of 30.6°) tested by Zheltovodov [7]. Unfortunately, the same modified $k-\omega$ turbulence model was failed to predict the secondary separation for a double-fin configuration at moderate crossing shock strength [5]. For double-fin case, Panaras [11] continued to apply modified BL model for $15^\circ \times 15^\circ$ wedge angle with Mach 3.85 incoming flow experimentally tested by Settles and Garrison [12] in success. More recently Schmisser and Gaitonde [13] and Panaras [14] numerically studied a double-fin configuration of $18^\circ \times 18^\circ$ and $23^\circ \times 23^\circ$ at Mach 5 experimentally investigated by Schülein and Zheltovodov [15]. These numerical studies have confirmed the experimental observations on the appearance, disappearance and reappearance of a secondary separation line, while strength of SWTBLI increases from moderate, strong to very strong levels.

In this study, numerical analyses will be carried out for a symmetrical double-fin configuration with fin inclination angle of 15° at a free-stream Mach 3.92 flow using steady RANS computational fluid dynamics (CFD) approach with turbulence models up to the second-moment closure, i.e. the ω -based Reynolds Stress equation model (RSM). First, for the $15^\circ \times 15^\circ$ DF configuration, the Reynolds Stress Model will be assessed against experiment, along with one-equation Eddy Viscosity Transport (EVT) model of Menter [16], and two-equation Shear Stress Transport (SST) model of Menter [16, 17]. CFD results will be compared with available experimental data [18] and previous numerical investigations [4, 5]. Second, emphasize will be placed on the mean surface flow topology transformation by adopting different turbulence models. Predicted flow fields will be compared qualitatively with available experiments [15, 18] and other relevant studies [4, 5, 11, 14, 19, 20], in particular the prediction of secondary separation phenomenon at moderate interactions. This will be carefully examined and assessed with different turbulence models. Finally, flow structures and 3-D separation characteristics will be presented, along with the flow pattern on the fin sidewalls, in an attempt to have in-depth understanding of complex 3-D flow topology in present double-fin configuration.

2. PHYSICAL PROBLEM AND NUMERICAL TREATMENT

2.1. Configuration

Figure 1 above gives a sketch of double sharp fins mounted on a flat plate with incoming supersonic turbulent boundary-layer flow. While approaching the sharp fin leading-edges, the incoming supersonic flow will be deflected, generating two crossing shock waves at a strength dependent on the free-stream Mach number (M_∞) and the fin inclination angles (β_1, β_2). At the rear of the fin shoulders and downstream of the fin trailing-edges (see Figure 2), the flow will undergo the so-called Prandtl-Meyer expansion, similar to that seen in expansion-compression corner. Between the fins, crossing shock waves will interact with 3-D spatially-developing turbulent boundary layer, and for strong interactions

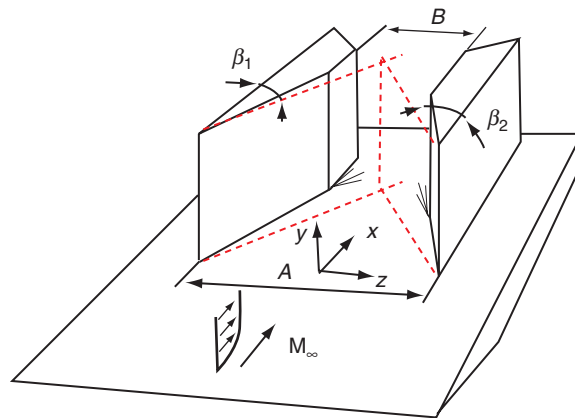


Figure 1. A sketch of double sharp fins (DF) mounted on a flat plate with incoming supersonic turbulent boundary-layer.

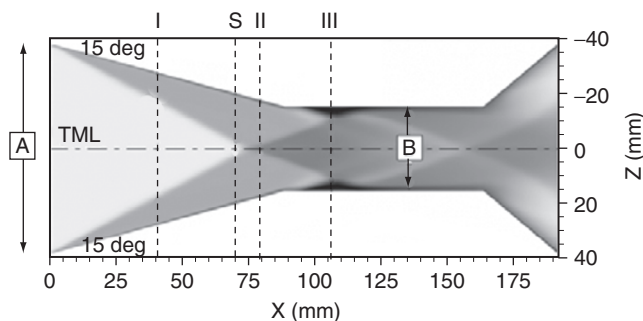


Figure 2. A 15° × 15° double fin (DF) flow configuration, superimposed by computed Mach number contours in the inviscid flow regions.

of high adverse pressure gradient, flow separation will occur in the near wall region, leading to a complex flow structures that will have subsequently impact on key parameters such as skin friction and wall heat flux coefficients.

Symmetrical double fin configuration at wedge angles ($\beta_1 = \beta_2$) of 15°, representing a moderate shock interaction, will be considered in the present study. A computational domain corresponds to a previous experiment [18], where two symmetrical chamfered sharp fins of 192 mm in length and 100 mm in height were mounted on a flat plate. The minimum throat distance (B) and the inlet width (A) depicted in Figure 2 are 32 mm and 79.1 mm, respectively. Same as numerical study of Thivet et al. [4, 5], a shorter height of 80 mm is used, based on the fact that no significant vertical gradients were experimentally observed in the region of $y = 70 - 90$ mm. Figure 2 also illustrates the throat middle line (TML) along the bottom wall and three cross-section locations at $x = 46$ mm, 79 mm and 112 mm, measured from the fin leading-edge (marked as I, II and III, respectively), where comparisons of computation and experiment will be made. The cross-section ‘S’ ($x = 70$ mm) corresponds to $x/\delta = 20$ and will be used to assess the secondary separation phenomenon where $\delta = 3.5$ mm is the boundary layer thickness measured at 14 mm upstream the fin leading edges. The coordinate system is shown in Figure 1, with x the stream-wise, y the wall-normal, and z the span-wise directions, respectively.

2.2. Numerical method

The 3-D compressible RANS governing equations with low-Re treatment are solved in physical flow domain using an unstructured grid finite-volume solver with second-order numerical scheme in time and space. A MUSCL-type re-construction with the min-mod limiter is used for shock-capturing. Simulations are run as steady RANS with three turbulence models as second-moment closure ω -based Reynolds Stress equation turbulence model (RSM), one-equation Eddy Viscosity Transport (EVT) equation model and two-equation Shear Stress transport (SST) model, respectively.

Table 1. Grid parameters

Grid	$N_x \times N_y \times N_z$ ^a	Δy_1 (μm) ^b	Δy_1 ^{+c}	Δz_1 (μm) ^d	Δz_{TML} (mm) ^e
Coarse	180 × 26 × 25	4.50	1.80 – 9.20	11.30	0.69
Medium	180 × 52 × 50	2.10	0.80 – 3.90	5.60	0.41
Fine	180 × 104 × 100	0.60	0.10 – 1.10	2.70	0.19
Very Fine	180 × 120 × 120	0.10	0.02 – 0.20	2.60	0.05

^a Number of grid points in the stream-wise (x), the wall-normal (y) and the span-wise (z), respectively; ^b The first cell height from the bottom wall; ^c A range of y^+ at the bottom wall; ^d The first cell height from the fin sidewalls; ^e The first cell height from the symmetry plane at the TML.

2.3. Flow conditions and meshing

The experimental free-stream incoming Mach number and stagnation conditions are $M_\infty = 3.92$, total pressure $P_0 = 1485$ KPa, and total temperature $T_0 = 260$ K, respectively, yielding a unit Reynolds number of $Re_1 = 88 \times 10^6 \text{ m}^{-1}$ [18]. A precursor turbulent boundary-layer flow computation was performed to evaluate a streamwise distance to the flat plate leading-edge where the predicted mean turbulent boundary-layer thicknesses δ and the momentum thickness θ match the experimental measurements of $\delta = 3.5$ mm and $\theta = 0.128$ mm [18], respectively. Thus, the Reynolds numbers $Re_\delta = 3.08 \times 10^5$ and $Re_\theta = 1.126 \times 10^4$ have been realized in the experiment. The fin is then located at 4δ downstream of this location to its leading-edge. This results in a distance of 168 mm upstream of the fin leading-edge. There is no consideration of chemical dissociation of air which typically occurs in hypersonic flows and the fluid is assumed to be an ideal gas with specific heat at constant pressure (C_p) kept as $1020 \text{ J kg}^{-1} \text{ K}^{-1}$ considering an air flow in the test. Supersonic characteristic flow condition is applied at the outflow. Due to the inherent symmetry of the flow domain and for steady flow simulation, only half a computational domain was used, similar to other studies [4, 5, 6, 13]. At the top boundary a free-slip condition is applied, and the bottom wall and fin sidewalls apply no-slip conditions.

Grid convergence studies were performed previously on three successive structured grids ranging from coarse to fine (for details, see Yao et al. [19]), with near-wall resolutions similar to an earlier study done by Thivet et al. [4, 5] using the same configuration. An additional very fine grid was introduced in this study to ensure grid-independence being achieved for all models. Table 1 gives a summary of the grid parameters for the $15^\circ \times 15^\circ$ DF configuration. The number of grid points in the stream-wise direction (N_x) is kept constant, while further refining grid points in both the wall normal (N_y), and the span-wise (N_z) directions. It was found that sufficient grid points were required in the region of the primary crossing shock wave interactions along the Throat Middle Line (TML), where flow structure and wall heat fluxes were found to be significantly sensitive to grid resolutions and its quality.

In all simulations, a convergence criterion of 10^{-5} in terms of root-mean-square (RMS) residual is defined with a default number of interactions of 250. The solution convergence is also determined by monitoring the surface pressure, skin friction and the wall heat flux coefficients on a wide range of monitoring (probe) points on the bottom wall. Simulation time varies with the very fine grid calculation requiring about 96 hours CPU time on a desktop P4 computer.

3. RESULTS AND DISCUSSIONS

Computed results of the $15^\circ \times 15^\circ$ double-fin configuration will be assessed and discussed with available experimental measurements and previous numerical investigations, in terms of wall pressure distributions, surface flow topology/pattern, secondary separation phenomena, and vorticity features as described below.

3.1. Validation of wall pressure distributions

Wall pressure distribution is an important indicator of turbulence model performance in predicting high Reynolds number viscous-inviscid interactions. Figure 3 shows the computed wall static pressure distributions by three turbulence models (EVT, SST and RSM), in comparison with experimental measurement of Zheltovodov et al. [18] and numerical predictions of Thivet et al. [4, 5] along the Throat Middle Line (TML) and three cross-section lines I, II and III. The inviscid shock relations in terms of pressure jump at TML and sections I and II are also plotted on the same figure for reference. Grid refinement studies were carried out and results have been reported in Yao et al. [19]. Here, only results from the very fine grid (see Table 1) are presented and normalised wall pressure (P/P_1), where

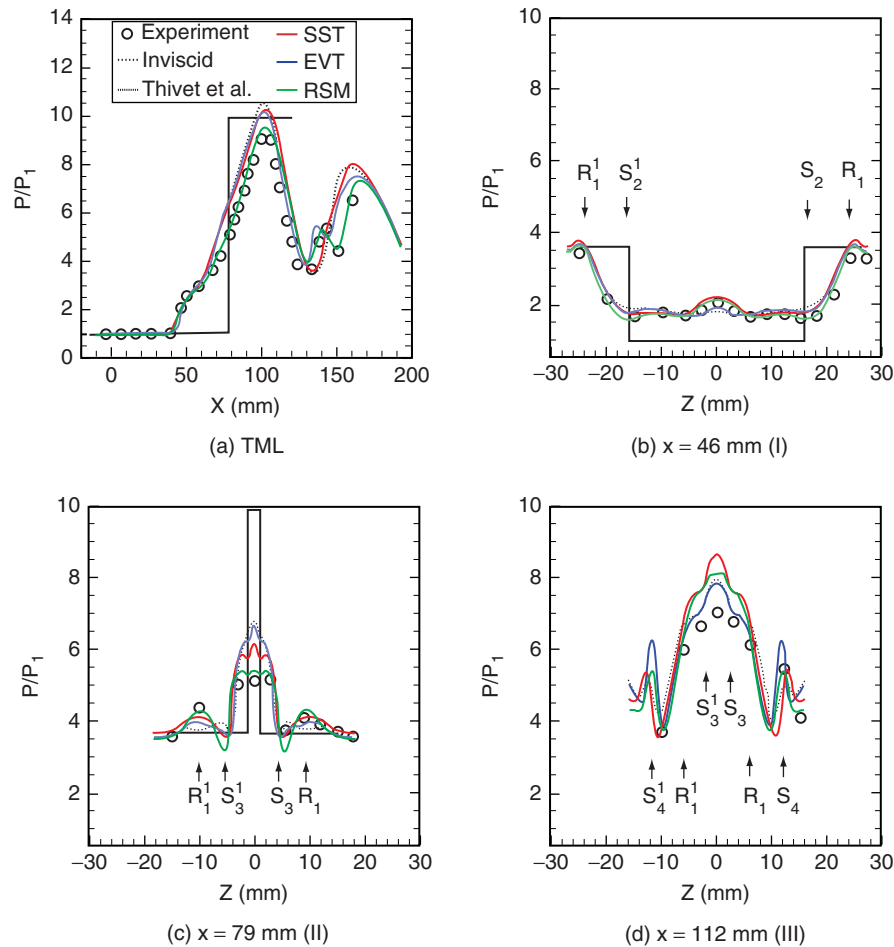


Figure 3. Comparison of normalised wall static pressure distributions (P/P_1) along the TML and three cross-sections I, II, III.

P_1 denotes the undisturbed free-stream wall pressure) variations are validated against test data. Along the TML (see Figure 3a), results from EVT and SST models over-predict the first peak pressure, similar to that of Thivet [4, 5] who used $k-\omega$ turbulence model. Downstream after the interaction, all three model results are able to predict the rapid pressure drop due to expansion wave around fin shoulders, but unable to capture the second pressure drop occurred at $x = 150$ mm in experiment. Overall, result from the RSM model shows much better agreement with the experimental data over EVT and SST models, in terms of predicting the first peak pressure at $x = 100$ mm and the second pressure drop at $x = 150$ mm. Comparisons at two cross-section lines I (Figure 3b) and II (Figure 3c) show that results from EVT model agree well with that of Thivet et al. [4, 5] and both slightly under-predict the centreline pressure at position I, but over-predict at position II. By using SST model, predictions improve slightly at position I, but not at position II where it still over-predicts. Results from RSM model have shown overall good agreement with test data at both positions I and II. At downstream position III (Figure 3d), EVT model gives better prediction in TML region, while RSM model better predicts outer region close to fin walls, in agreement with test data. Labels S_1, R_1, S_3 and their counterpart with the superscript '1' represent primary separation, primary reattachment, and secondary separation lines predicted with RSM model. Details discussion will be given below.

3.2. Surface flow pattern

Figures 4 and 5 show the experimental oil-flow visualisations [18] compared with the computed limiting flow pattern using RSM turbulence model, and Figure 6 depicts the computed flow topology using SST and EVT turbulence models, respectively. The computed surface flow patterns are generated with wall shear streamlines at the bottom wall.

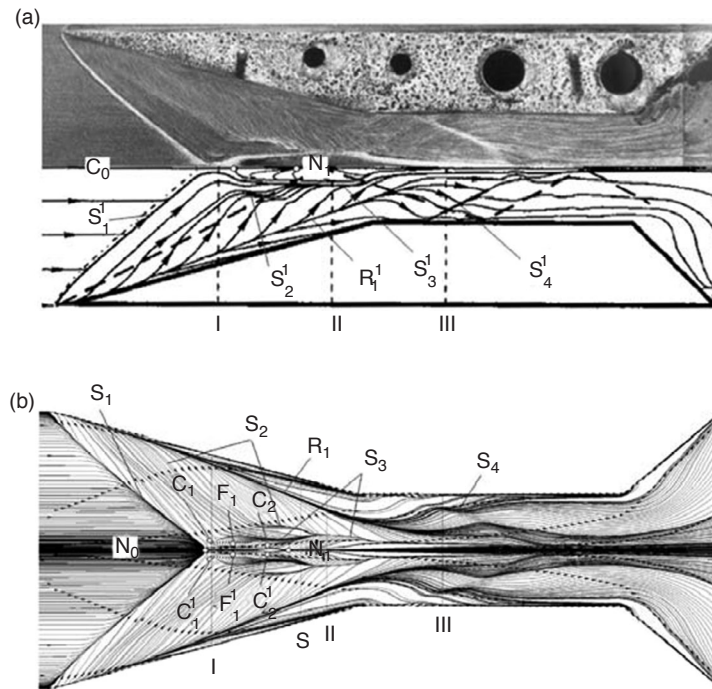


Figure 4. Surface flow pattern of experimental observation (a) and computational prediction by RSM turbulence model (b).

For clarity, the following notations are adopted; i.e. ‘S’ and ‘R’ stand for separation (convergence) and reattachment (divergence) lines, whereas singular points are denoted with ‘C’ (saddle), ‘N’ (node), and ‘F’ (focus), respectively. Symmetric counterpart (i.e. lower-half in each picture) is featured with the superscript ‘1’ and arrows define the flow directions. Note that the well-known topological rule of thumb requiring equality of node and saddle points will be applied to analysis figures below.

As shown in Figure 4a, at the channel entrance, the swept shock waves generated by the two sharp fins interact with a spatially-developing supersonic turbulent boundary layer along the flat plate. Due to strong inviscid/viscous interactions, the boundary layer separates along the convergence line S_1^1 , and reattaches to the divergence line R_1^1 , forming a counter-rotating vortex pair (CRVP) which develops further downstream. In the meantime, the shock-shock interaction occurs at the throat middle line, inducing a large scale central separation zone (subject to level of adverse pressure gradient) behind the centreline saddle point C_0 and bounded by the separation lines S_3 and S_3^1 as observed in experiment (Figure 4a and Figure 5a). For a moderate interaction, increased flow entrainment from the divergence line R_1^1 towards the convergence line S_1^1 could induce the formation of the so-called secondary separation line S_2^1 in the vicinity of the central separation zone shown in figures 4 and 5. The secondary separation lines eventually merge with the primary separation lines S_1, S_1^1 downstream in the middle of the central separation zone (i.e. $x \approx 70$ mm).

The computed surface flow pattern using the RSM turbulence model (Figures 4b) is qualitatively in good agreement with the experimental oil-flow visualisations shown in Figure 4a. In particular, primary separation and attachment limiting streamlines (S_1 and R_1), as well as the separation line S_4 resulting from the interaction of reflected shock with expansion fan originated from the fin shoulder is well captured by this model. However, there are still some differences by comparing further details around the central separation zone (depicted in Figure 5b). CFD results show that the primary separation lines S_1 and S_1^1 intersect with the centreline at a node point N_0 , and therefore no fluidic-throat being formed between these two lines. This finding agrees with previous studies for the same problem ([4, 11, 18, 19, 20, 21]). It is noteworthy to emphasise here that the penetrating liquid-throat was observed between the primary separation lines (see Figures 4a and 5a) in the experiment where unsteady and intermittent separation occurred in the vicinity of the central separation point in the real flow. Therefore it cannot be accurately captured by steady RANS computations. Nevertheless, the secondary separation line (S_2),

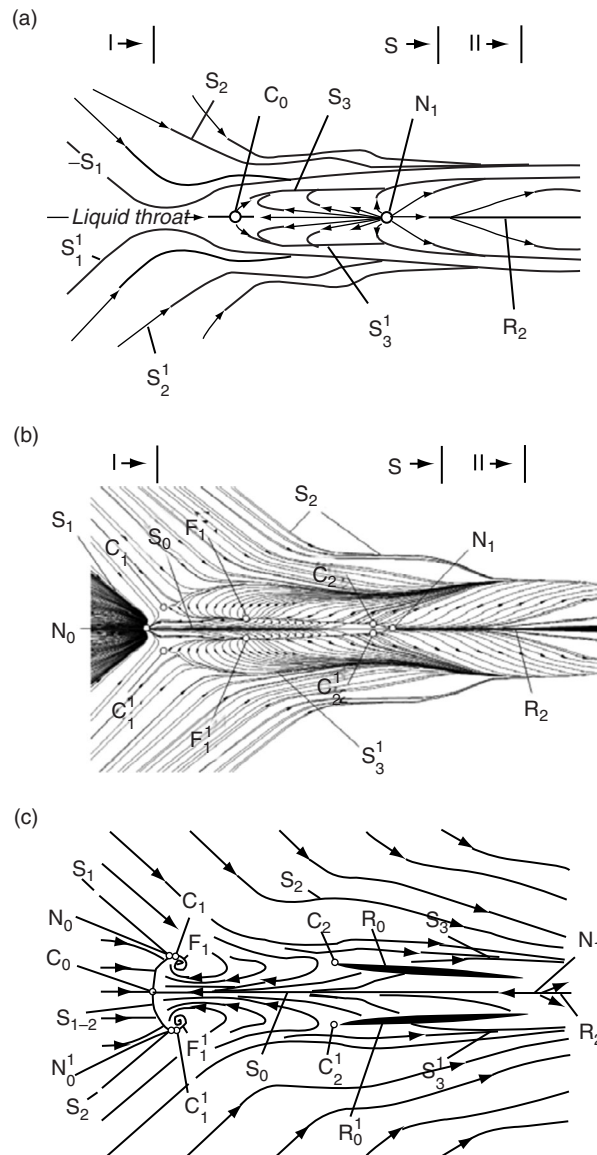


Figure 5. Enlarged central separation zone showing detailed surface flow pattern of experiment (a), computation with RSM turbulence model (b) for a $15^\circ \times 15^\circ$ double-fin at Mach 3.92, and experiment (c) for a $18^\circ \times 18^\circ$ double-fin at Mach 5 [15].

which was clearly evident from the experimental oil-flow visualisations has been reproduced by the RSM turbulence model. CFD modelling also predicted some additional flow features that were not observed in the experiment; e.g. two saddle points C_1 and C_1^1 located symmetrically against the throat middle line. Thus, a diamond-shaped flow pattern with points $(N_0, C_1, C_1^1, \text{ and } N_1)$ is present, along with two repelling focus points F_1 (and its symmetrical counterpart F_1^1) instead of the saddle C_0 as seen in the experiment. In addition, two new saddle points C_2 and C_2^1 are captured slightly ahead of a central node point N_1 . As shown in Figure 5b, the location of two focus points (F_1 and F_1^1) matches the position of an experimental saddle point C_0 (see Figure 5a). Similarly, there is a good agreement between the measured and computed locations of a centreline node point N_1 . The existence of two side divergence lines (R_0 and its symmetrical counterpart R_0^1) are evident, and they start from the focus points F_1 (and F_1^1) and end at the saddle points C_2 and C_2^1 very close to the central node point N_1 . Similar divergence lines are also directed from the focus points F_1 (and F_1^1) to the saddle points C_1 and C_2^1 . The central coalescence line S_0 which joins the nodes points N_0 and N_1 is also numerically predicted, but not observed in experiment, possibly due to the flow unsteadiness and intermittency as discussed above.

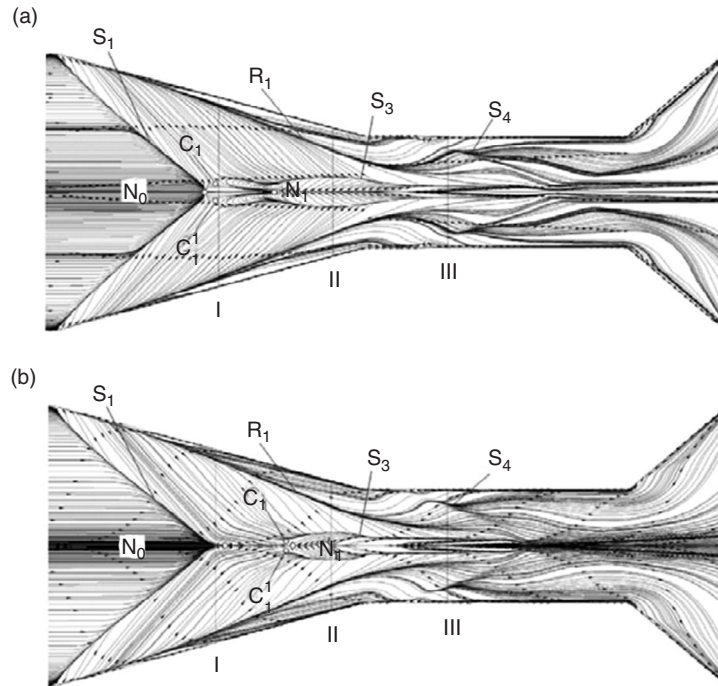


Figure 6. Computed surface flow pattern with (a) SST turbulence model, and (b) EVT turbulence model.

It is also worth highlighting here that predicted specific flow pattern was somewhat closer to that observed in the stronger Mach 5, $18^\circ \times 18^\circ$ double-fin case tested by Schülein and Zheltovodov [15] (see Figure 5c). Particularly, the reversed flow with the central coalescence line S_0 directed from the node point N_1 was found in opposite direction to the central divergence line R_2 as well as two symmetrically stretched regions R_0 and R_0^1 corresponding to predicted divergence lines observed in experiment. However, two saddle points C_2 and C_2^1 located in the apexes of the divergence lines have been identified by surface flow pattern visualization instead of predicted focus points. The saddle point C_0 observed in experiment in the centre of cross-separation line S_{1-2} instead of predicted node N_0 . The pairs of additional symmetric node points (N_0 and N_0^1), saddle points (C_1 and C_1^1) and focus points (F_1 and F_1^1) located on the sides of the line S_{1-2} characterize this flow topology.

Figure 6 gives RANS results by SST and EVT turbulence models, in which the primary separation and reattachment limiting lines (S_1 and R_1) are also captured, as well as the separation line S_4 resulting from the interaction of the reflected shock waves with the expansion waves. A diamond-shaped flow pattern with points (N_0 , C_1 , C_1^1 , and N_1) is present in all these cases. However, the large scale central separation zone bounded by two convergence lines S_3 and S_3^1 changes with different turbulence models adopted. For example, EVT turbulence model (Figure 6b) predicts two saddle points C_1 and C_1^1 further downstream close to the node point N_1 , compared to that by RSM and SST turbulence models. Despite the narrower central separation region than that observed in the experiments, EVT model predicts the closest location of the node point N_0 compared to the experimental C_0 among all three models tested. Unfortunately, no ‘liquid throat’ was captured by all three models considered.

In accordance with Figure 7, the surface skin friction $C_f = 0$ line is predicted by all three turbulence models used, showing those nodal points located on TML line as well as the reverse flow region between those points where $C_f < 0$. The zero skin friction value corresponds to the criterion of singular separation as contrasted with ordinary (or regular) separation arising at any locally minimal but positive values ($C_f > 0$). Further discussion of the primary and the secondary convergence lines will be given below.

3.3. Secondary separation

In order to reproduce correctly the inherent flow physics, secondary separation phenomenon should be captured numerically, e.g. by Panaras [8, 11] using a modified algebraic Baldwin-Lomax

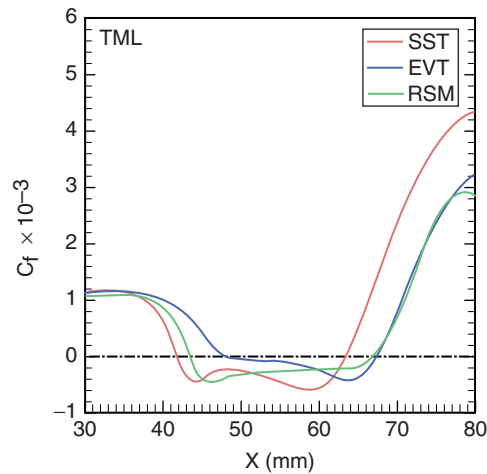


Figure 7. Skin friction coefficient distributions along the TML for the 15° x 15° case predicted by three different turbulence models.

turbulence model, which restricts the turbulence eddy viscosity (hence turbulence stress) in the cross-flow separation region to permit a pseudo-laminar flow separation. This physical phenomenon was explained by Zheltovodov on the basis of single-fin (SF) experiments [7, 22, 23] and catalogued in a total of six regimes for the 3-D single-fin flow field depending on the strength of the shock wave (Figure 8) (see also [1, 2, 3]). It was concluded that secondary separation initially appears when the interaction achieves a certain strength corresponding to some critical values of the fin deflection angle β_{ss}^* (Figure 8a) shown in the conical region (Figure 8b, sub-regime IIIa) but not in the inception region (i.e. the initial region of deviation from conical behaviour). Its span-wise extent grows with increasing shock strength (IIIb), but gradually diminishes, eventually appearing only in the inception region close to the fin apex (IV) and then disappearing altogether (V). Secondary separation does reappear in the strongest interaction but at a different position, closer to the fin than previously scenario (VI).

In accordance with researches by Zheltovodov [7, 22] as well as by Zubin and Ostapenko [24], it was concluded that the appearance, disappearance and re-appearance of secondary separation phenomenon in regimes III-VI are determined by two major factors: (1) the state (laminar or turbulent) of the ‘reverse’ cross-flow between primary-reattachment and separation lines; and (2) the acceleration

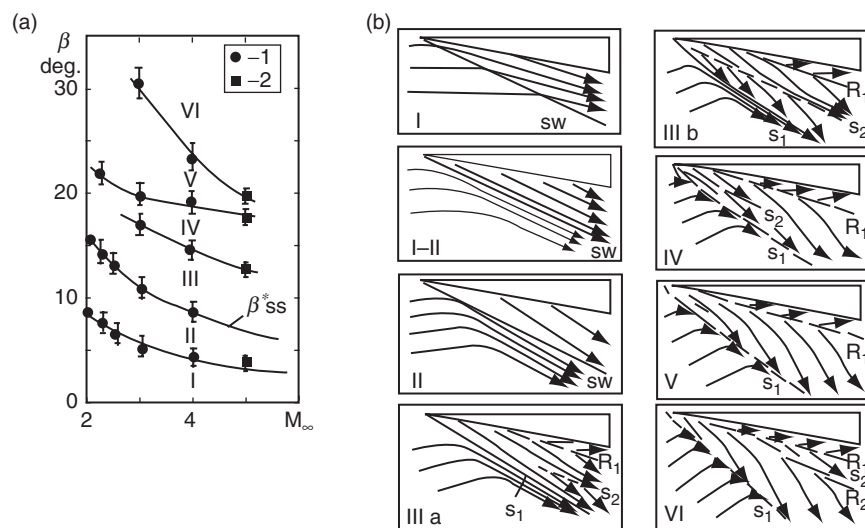


Figure 8. Classification of secondary separation regime from single sharp fin experiments [7].

of the near-wall cross-flow from subsonic to supersonic regions. Zheltovodov et al. [23] further demonstrated the suppression of the secondary separation in regimes III and IV (respectively, mild-moderate interaction cases) but not in very strong-interaction regime VI by ‘turbulizing’ the flow with sand-grain roughness applied along the reattachment line R_1 to trigger transition of the ‘reversed’ cross-flow. These experiments supported the hypothesis [7], that the behaviour of the secondary separation is initially related to laminar and transitional flow, and later to turbulent ‘reverse’ cross-flow in the swept separation bubble. Thus, the secondary separation phenomenon initially appeared in regime III and continuously existed in regime IV is in fact due to the subsonic laminar state of the near-wall ‘reverse’ cross-flow between primary separation and reattachment lines. Then, it starts to diminish in regime IV due to laminar-turbulent transition of the subsonic cross-flow and fully disappears in strong interaction regime V due to the achievement of the supersonic cross-flow state. The re-appearance of secondary separation in regime VI occurs at very strong interaction condition in the vicinity of the embedded normal shock wave with the critical strength ($\xi_1^* \geq 1.5-1.6$) which is typical for turbulent-reversed flow [7, 23].

Similar to single-fin studies of Panaras [8, 11], present investigation of a $15^\circ \times 15^\circ$ double sharp fin configuration aims to assess the capability of three turbulence models (RSM, SST, EVT) in capturing the regime III type secondary separation phenomenon in double-fin configuration. Figures 4 and 5 above have shown that RANS modelling with all three turbulence models tested is able to reproduce the second separation phenomenon. In particular, results produced by RSM turbulence model are qualitatively in better agreement with experimental observations [7, 22, 23].

Numerical analysis continues by focussing on a cross-section ‘S’ in the middle of the central separation zone; i.e. $x = 70$ mm, in order to understanding flow properties distribution in the lateral direction. Figure 9 shows skin friction coefficient (C_f) and pressure gradient component ($\partial p/\partial z$) predicted by three turbulence models. While all model results give broadly similar trend, details are different, particular at separation and reattachment locations. For example, the RSM model result exhibits a local minimum skin friction ($C_f = 1 \times 10^{-3}$) at the outside edge of the separation bubble. It then increases to a local maximum ($C_f = 2.4 \times 10^{-3}$) at a location where separation line S_3 occurs. After that, it decreases again to another local minimum ($C_f = 1.8 \times 10^{-3}$) in align with the secondary separation line S_2 located at $z = 6.6$ mm, before increasing to a maximum peak of 5×10^{-3} at the reattachment line R_1 .

The skin friction predicted by EVT and SST models has similar trend to that predicted by RSM model, but are less effective in capturing local minimum and maximum values. The distribution of pressure gradient ($\partial p/\partial z$) (Figure 9b) shows clear differences between results predicted by three models. Compared to predictions by SST and EVT models, the computed pressure gradient component by the RSM model has shown large variation at the locations of two separation lines S_2 , S_3 , before increasing monotonically towards the reattachment line (R_1). The difference of pressure

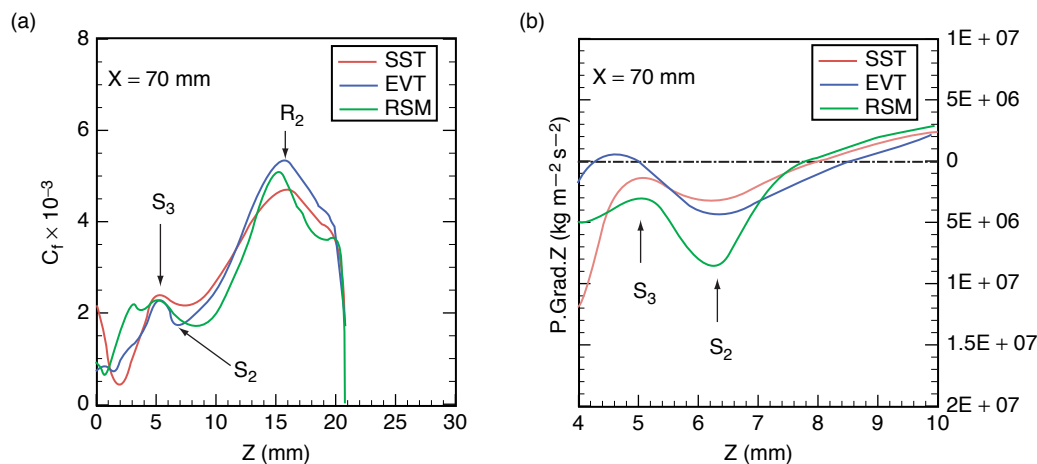


Figure 9. Computed skin friction coefficient (a) and pressure gradient component (b) at the section ‘S’ ($x = 70$ mm) by three turbulence models.

gradient between two local peaks at locations S_3 ($z = 5-5.2$ mm) and S_2 ($z = 6.4-6.6$ mm) is $5.4 \times 10^6 \text{ kg m}^{-2} \text{ s}^{-2}$, and this level of adverse pressure gradient contributes to appearance of secondary separation, similar to regime III of single-fin configuration (Figure 8).

Figure 10 shows the computed turbulence kinetic energy (TKE) distribution and vorticity surface streamlines at a cross-section ‘S’ (i.e. $x = 70$ mm), where the predicted TKE by RSM model has magnitude almost two-orders smaller than that by SST model. The higher TKE levels predicted by the SST model will cause ‘turbulization’ of the reversed flow, thus weakening or even preventing secondary separation phenomenon. In contrary, the RSM model predicts low level of TKE in the same region, and this permits the prediction of moderate secondary flow separation in the vicinity of the fin sidewall and underneath the primary cross-flow vortex, similar to that observed in the single-fin case. The flow pattern by RSM model depicted in Figure 10 shows a vortex core embedded in the inner turbulent part of turbulent boundary-layer, in agreement with previous numerical investigations by Panaras [8, 11].

The streamwise evolution of secondary separation predicted by the RSM model is shown in Figure 11 with computed vorticity streamlines at four successive cross-sections of I ($x = 46$ mm), $x = 59$ mm, II ($x = 79$ mm) and S ($x = 70$ mm), respectively. At position I and in the vicinity of the wall, the change of vorticity streamlines starts to trigger an initially weak vortical structure embedded underneath the main vortex-core. Further downstream at $x = 59$ mm, high vorticity level is predicted in a region just above the secondary separation line where a focus point appears at a vertical height of 0.4δ . This vortical pattern is

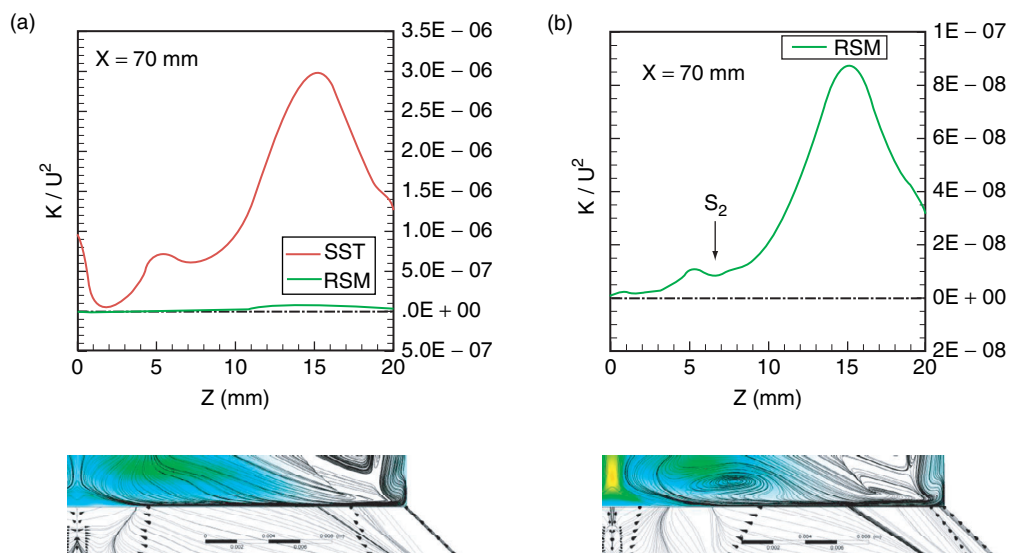


Figure 10. Distribution of normalised TKE: SST (a), RSM (b) with vorticity surface streamlines shown in vertical plane ($y = 0.8\delta$) and wall shear streamlines at the bottom wall.

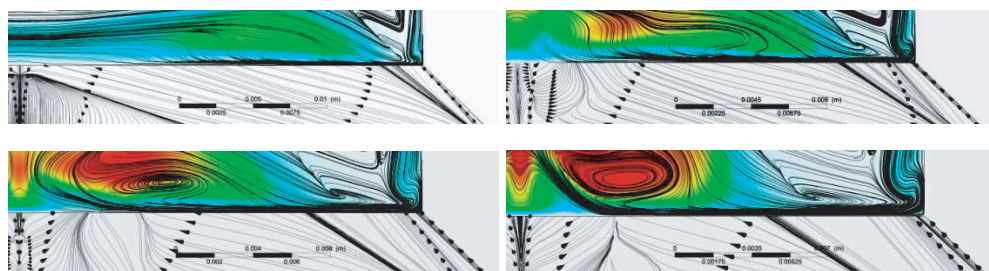


Figure 11. Computed vorticity streamlines superimposed by eddy viscosity contours by RSM model. From top to bottom (in clockwise): cross-sections I, $x = 59$ mm, II, and S ($x = 70$ mm).

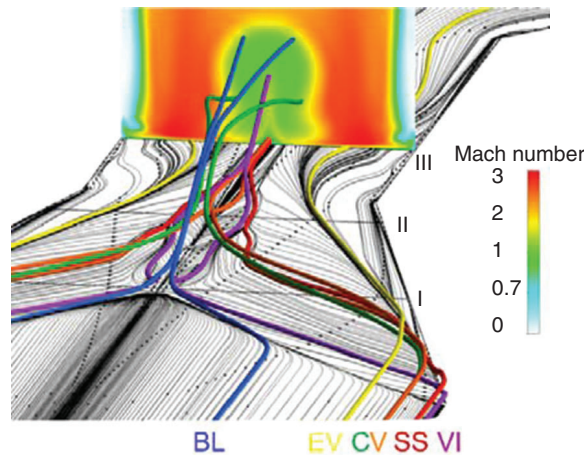


Figure 12. Computed flow regimes and 3-D streamline trace around separation by RSM model.

further strengthened in the span-wise while approaching to the middle throat region until it merges with the separation line S_3 ($x = 72\text{--}74$ mm). These observations agree with that shown in Figure 12 below (i.e. streamlines in ‘red’ and ‘violet’ colours).

Figure 12 depicts evolution of 3-D streamline trace and four salient coherent features, or flow regimes, in a similar manner as that described by Gaitonde and Shang [6]. Due to the strong adverse pressure gradient (APG) encountered downstream of the crossing-shock-wave location, the fluid lifts up along the primary separation lines without reattaching to the wall throughout the domain. The entire incoming boundary-layer and the fluid originated in the free-stream become engulfed in the separated region. As a result, a large low Mach number and high total pressure region will occupy a significant part of the outlet region (see Figure 12). The Vortex Interaction (VI) regime is characterized by the fluid that reattaches near the fin and sweeps in the span-wise to fill the void left by the separated boundary-layer fluid. The Centreline Vortex (CV) regime is outlined by a counter-rotating vortex pair around the centreline represented by ‘green’ and ‘orange’ coloured streamlines. The fluid attached further downstream before the symmetry plane forms the Entrainment Flow (EF) which brings high-momentum fluid near the wall. Additionally, present computations showed that the Secondary Separation (SS) is located in the near-wall region ($y = 0.01$ mm) underneath the CV coherent feature. This suggests that, in order to capture the secondary separation phenomenon, the near-wall grid size has to be smaller than this value. While approaching to the central separated region, SS first merged with the VI regime and later with the CV regime downstream.

3.4. Flow structure at the fin sidewall

Figures 13a and 13b give the experimentally observed flow structure on the fin sidewalls [18]. A large separation region was detected between the separation line S_9 and the reattachment line R_9 , and it was caused by the interaction of the reflected shock waves impinging onto the fin surface, together with the expansion waves resulting from the expansion corner of fin shoulder. Figure 13c gives the computational results with the limiting streamlines by RSM model confirmed the existence of the node point N_2 and the saddle point C_2 , as observed in the experiment [18] and previous studies [19, 21]. A large separation zone bounded by the separation line S_9 and the reattachment line R_9 is also detected in the region of incidence of the shock wave behind the fin shoulder. As observed in the experiment, present computations detect a saddle point C_3 and a focus point F_1 in the near wall region, along with a saddle point C_2 and a node point N_2 , away from the wall. However, the computed separation line S_9 is located slightly downstream than in the experiments. Figure 14 depicts the presence of the swirling vortex originated at the base point from a focus F_1 and then propagated vertically upwards, from both experimental measurement and computational result. The longitudinal vortex (denoted ‘2’ in Figure 14a) is also captured by present computations, showing a bounding envelope around a vortex core (Figure 14b).

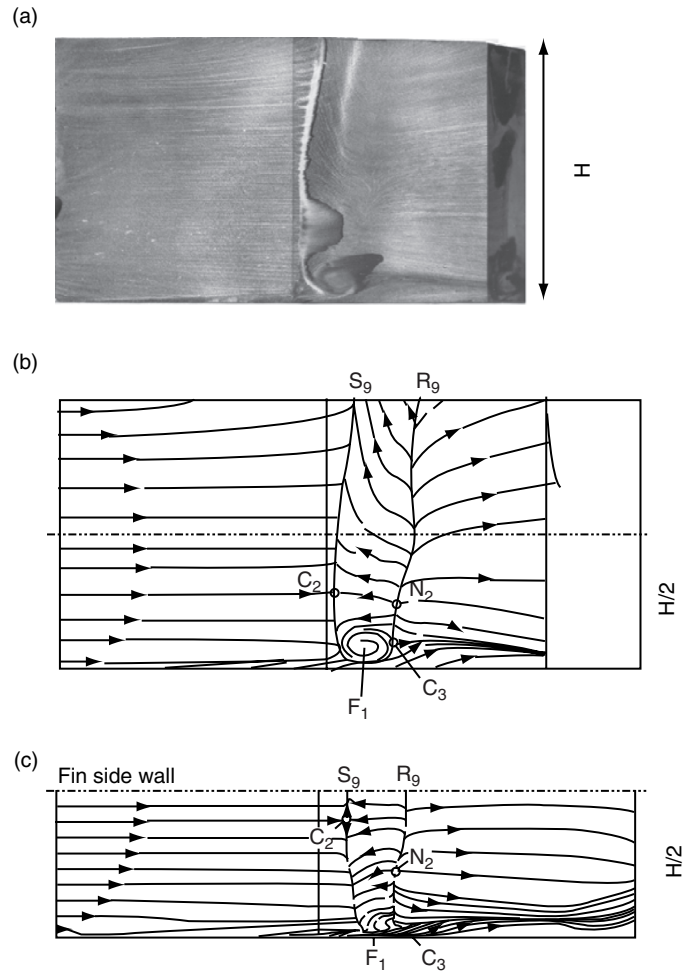


Figure 13. Flow pattern at the fin sidewall: experiment (a, b); computation by RSM model (c).

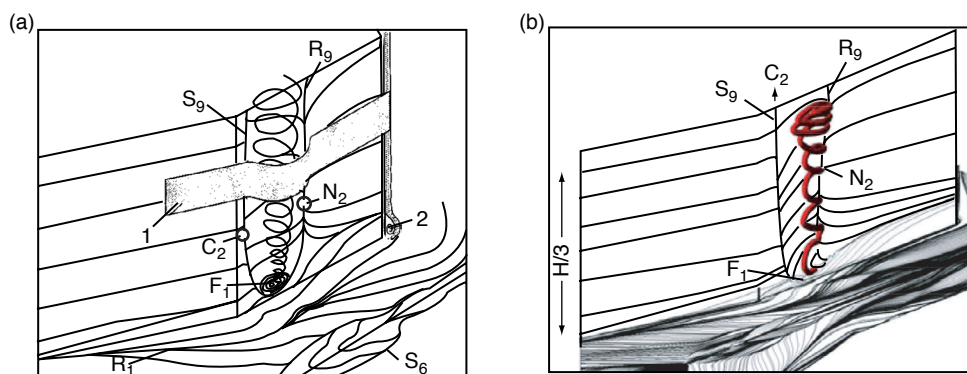


Figure 14. Flow structure on the fin sidewalls caused by vortex/sidewall interactions: experiment [18] (a); computation by RSM model (b).

4. CONCLUSIONS

The crossing shock-wave and turbulent boundary-layer interactions have been carried out for a supersonic turbulence boundary-layer flow over a symmetric double sharp fin configuration at a fin inclination angle of 15° and free-stream Mach 3.92, using steady RANS modelling approach with three turbulence models as the ω -based Reynolds Stress equation model (RSM), the one-equation Eddy

Viscosity Transport (EVT) and the two-equation Shear Stress Transport (SST). Comparisons of predicted wall pressure distribution along the throat middle line and three successive cross-section lines have shown good agreement with available experimental measurement, of which results from RSM model gave better agreement over other two models. It was also found that mean surface flow patterns computed with RSM model were in good qualitative agreement with experimental oil-flow visualizations, despite that detailed flow topology at the central separation zone was different to the experimental test where unsteadiness and intermittency were co-exist in the real flow. One unique feature in this type of interaction; i.e. the secondary separation initially observed in single sharp fin flow, has been successfully reproduced for the first time in a double sharp fin configuration by numerical computation using the RSM model. Comparing to other two models, the RSM model is able to predict correct level of TKE that is crucial for determining the pseudo-laminar state of an embedded reversed flow underneath the main cross-flow vortex. Further studies on turbulence kinetic energy, skin friction coefficient, pressure gradient, and vorticity distributions show consistent features of local minimum and maximum peaks, in correspondence of the secondary separation lines. Three-dimensional flow structure analysis suggested that secondary separation was weak initially, and then strengthened particularly in the span-wise towards the central separation zone where it merged with the Vortex Interaction flow, and with the Centreline Interaction flow further downstream. Further investigations are needed to determine the correct level of turbulence production/dissipation and also to consider flow unsteadiness and intermittency effect by using unsteady RANS with suitable transitional turbulence model.

ACKNOWLEDGEMENTS

The first author would like to acknowledge the Graduate Teaching Assistantship provided by Kingston University London.

REFERENCES

- [1] Knight, D.D., Yan, H., Panaras, A.G. and Zheltovodov, A.A., Advances in CFD prediction of shock wave turbulent boundary layer interactions, *Progress in Aerospace Sciences*, 2003, 39(2–3), 121–184.
- [2] Zheltovodov, A.A., Some advances in research of shock wave turbulent boundary layer interactions, AIAA Paper, 2006, 0496.
- [3] Zheltovodov, A.A. and Knight, D.D., Ideal gas shock wave turbulent boundary layer interactions in supersonic flows and their modelling: three-dimensional interactions, in: Babinsky, H. and Harvey J.K. eds., *Shock Wave-Boundary-Layer Interactions*, Cambridge University Press, New York et al., 2011, 202–258.
- [4] Thivet, F., Knight, D.D. and Zheltovodov, A.A., Analysis of observed and computed crossing-shock-wave/turbulent-boundary-layer interactions, *Aerospace Science and Technology*, 2002, 6(1), 3–17.
- [5] Thivet, F., Knight, D.D., Zheltovodov, A.A. and Maksimov, A.I., Insights in turbulence modelling for crossing-shock-wave/boundary-layer interactions, *AIAA Journal*, 2001, 39(6), 985–995.
- [6] Gaitonde, D.V. and Shang, J.S., Structure of a turbulent double-fin interaction at Mach 4, *AIAA Journal*, 1995, 33(12), 2250–2258.
- [7] Zheltovodov, A.A., Regimes and properties of three-dimensional separation flow initiated by skewed compression shocks, *J. Appl. Mech. Tech. Phys.*, 1982, 23(3), 413–418.
- [8] Panaras, A.G., The effect of the structure of swept-shock-wave/turbulent-boundary-layer interactions on turbulence modelling, *J. Fluid Mech.*, 1997, 338, 203–230.
- [9] Durbin, P.A., On the $k-\epsilon$ stagnation point anomaly, *Int. J. Heat & Fluid Flow*, 1996, 17(1), 89–90.
- [10] Thivet, F., Knight, D., Zheltovodov, A.A. and Maksimov, A.I., Importance of limiting the turbulence stresses to predict 3D shock wave boundary layer interactions, *The 23rd International Symposium of Shock Waves*, Ft. Worth, TX, July 2001, Paper No. 2761.
- [11] Panaras, A.G., Algebraic turbulence modelling for swept shock-wave/turbulent boundary-layer interactions, *AIAA Journal*, 1997, 35(3), 456–463.

- [12] Garrison, T.J., Settles, G.S., Narayanswami, N. and Knight, D.D., Laser Interferometer Skin-Friction Measurement of crossing-Shock-Wave/Turbulent-Boundary-Layer Interactions, *AIAA Journal*, 1994, 32(7), 1234–1241.
- [13] Schmisser, J.D. and Gaitonde, D.V., Numerical investigation of new topologies in strong crossing shock-wave/turbulent boundary-layer interactions, *AIAA Journal*, 2001, 39(19), 1742–1749.
- [14] Panaras, A.G., Calculations of flows characterized by extensive crossflow separation, *AIAA Journal*, 2004, 42(12), 2474–2481.
- [15] Schülein, E. and Zheltovodov, A.A., Development of experimental methods for the hypersonic flows studies in Ludwig tube, Proc. *International Conference on the Methods of Aerophysical Research*, 1998, Novosibirsk, Russia, Part I, 191–199.
- [16] Menter, F. R., Zonal Two Equation $k-\omega$ Turbulence Models for Aerodynamic Flows, AIAA Paper, 1993, 2906.
- [17] Menter, F.R., Two-Equation Eddy-Viscosity Turbulence Models for Engineering Applications, *AIAA Journal*, 1994, 32(8), 1598–1605.
- [18] Zheltovodov, A.A., Maksimov, A.I. and Shevchenko, A.M., Topology of three-dimensional separation under the conditions of symmetric interaction of crossing shocks and expansion waves with turbulent boundary layer, *Thermophysics and Aeromechanics*, 1998, 5(3), 293–312.
- [19] Yao, Y.F., Salin, A. and Lo, S.H., Numerical analysis of wall properties in cross shock wave and boundary layer interactions, AIAA Paper, 2011, 0860.
- [20] Zheltovodov, A.A., Maksimov, A.I., Gaitonde, D., Visbal, M.R. and Shang, J.S., Experimental and numerical study of symmetric interaction of crossing-shocks and expansion-waves with a turbulent boundary layer, *Thermophysics and Aeromechanics*, 2000, 7(2), 155–171.
- [21] Salin, A., Yao, Y.F. and Zheltovodov, A.A., Flow Topology of Symmetric Crossing Shock Wave Boundary Layer Interactions, in: Kontis K. ed., *Shock Waves*, Heidelberg: Springer, 2012, ISBN: 978-3-642-25687-5.
- [22] Zheltovodov, A.A., Physical features and properties of two- and three-dimensional separated flows at supersonic velocities, *Izvestiya AN SSSR, Mekhanika Zhidkosti i Gaza (Fluid Mechanics)*, 1979, 3, 42–50 (in Russian).
- [23] Zheltovodov, A.A., Maksimov, A.I., and Schülein, E., Development of turbulent separated flows in the vicinity of swept shock waves, in: Kharitonov A.M. ed., *Interaction of Complex 3-D Flows*, Novosibirsk, 1987, 67–91 (in Russian).
- [24] Zubin, M.A. and Ostapenko, N.A., Structure of the flow in the region of separation for interaction of a normal shock wave with normal shock wave with a boundary layer, *Izvestiya AN SSSR, Mekhanika Zhidkosti i Gaza (Fluid Mechanics)*, 1979, 3, 51–58 (in Russian).

